AGU PUBLICATIONS

JGR

Journal of Geophysical Research: Solid Earth

RESEARCH ARTICLE
10.1002/2016JB013739

Key Points:
- Tilt change during the 450 s before the 2014 phreatic eruption of Mount Ontake was analyzed to address eruption dynamics
- Tilt change was characterized by a linear function in time followed by exponential growth
- Results were modeled by cracking of an intact region by intense boiling of underground water

Correspondence to:
Y. Maeda,
maeda@seis.nagoya-u.ac.jp

Citation:
Maeda Y., A. Kato, and Y. Yamanaka (2017), Modeling the dynamics of a phreatic eruption based on a tilt observation: Barrier breakage leading to the 2014 eruption of Mount Ontake, Japan, *J. Geophys. Res. Solid Earth*, *122*, 1007–1024, doi:10.1002/2016JB013739.

Received 14 NOV 2016
Accepted 29 JAN 2017
Accepted article online 3 FEB 2017
Published online 18 FEB 2017

Modeling the dynamics of a phreatic eruption based on a tilt observation: Barrier breakage leading to the 2014 eruption of Mount Ontake, Japan

Yuta Maeda[1], **Aitaro Kato**[2], **and Yoshiko Yamanaka**[1]

[1]Graduate School of Environmental Studies, Nagoya University, Nagoya, Japan, [2]Earthquake Research Institute, University of Tokyo, Tokyo, Japan

Abstract Although phreatic eruptions are common volcanic phenomena that sometimes result in significant disasters, their dynamics are poorly understood. In this study, we address the dynamics of the phreatic eruption of Mount Ontake, Japan, in 2014 based on analyses of a tilt change observed immediately (450 s) before the eruption onset. We conducted two sets of analysis: a waveform inversion and a modified phase-space analysis. Our waveform inversion of the tilt signal points to a vertical tensile crack at a depth of 1100 m. Our modified phase-space analysis suggests that the tilt change was at first a linear function in time that then switched to exponential growth. We constructed simple analytical models to explain these temporal functions. The linear function was explained by the boiling of underground water controlled by a constant heat supply from a greater depth. The exponential function was explained by the decompression-induced boiling of water and the upward Darcy flow of the water vapor through a permeable region of small cracks that were newly created in response to ongoing boiling. We interpret that this region was intact prior to the start of the tilt change, and thus, it has acted as a permeability barrier for the upward migration of fluids; it was a breakage of this barrier that led to the eruption.

1. Introduction

Volcanoes exhibit both magmatic and phreatic eruptions. Most of the previously proposed models of eruption dynamics [e.g., *Melnik and Sparks*, 2005; *Anderson and Segall*, 2011; *Kozono and Koyaguchi*, 2012] have focused on magmatic eruptions. These magmatic eruption models are highly advanced, taking into account various elementary processes including nucleation and growth of gas bubbles in magma, vertical and lateral gas escape from the magma, and crystallization of the magma in the conduit. Compared with magmatic eruptions, the dynamics of phreatic eruptions has received less attention and is poorly understood, with very few previous modeling studies [e.g., *Germanovich and Lowell*, 1995]. Since phreatic eruptions are a common phenomenon in volcanoes and sometimes result in significant disasters [e.g., *Yamamoto et al.*, 1999], improving our understanding of phreatic eruption dynamics is essential to volcanology.

Eruption dynamics could be investigated not only by purely theoretical approaches but also by observation-based approaches. Especially promising are tilt observations made with tiltmeters that can record tilt changes as small as 10^{-9} rad at high (e.g., 1 Hz) sampling rate. Typical time scales of the tilt changes (several minutes to hours) align with those of immediate precursory processes at volcanoes [e.g., *Iguchi et al.*, 2008]. Several studies have used combined observation-modeling approaches to explain tilt changes associated with eruptions. For example, *Genco and Ripepe* [2010] observed that the tilt at Mount Stromboli, Italy, accelerated at 1.5 power of time before eruptions. They explained this observation by referring to the model of diffusive gas bubble growth in magma that had been developed by *Nishimura* [2009]. At Mount Semeru, Indonesia, *Nishimura et al.* [2012] showed that a tilt change accelerated before vulcanian eruptions but did not accelerate before gas bursts. These characteristics were attributed to constant gas supply from greater depths and gas escape through incompletely connected fractures in magma [*Nishimura et al.*, 2012]. At Kilauea, Hawaii, tilt changes associated with gas pistonings were analyzed by waveform inversion, leading to an interpretation that the gas pistonings were caused by repeated growth and collapse of a layer of foam [*Chouet and Dawson*, 2015]. These studies indicate that quantifying the waveform characteristics of tilt changes is a useful approach to improve our understanding of the eruption dynamics.

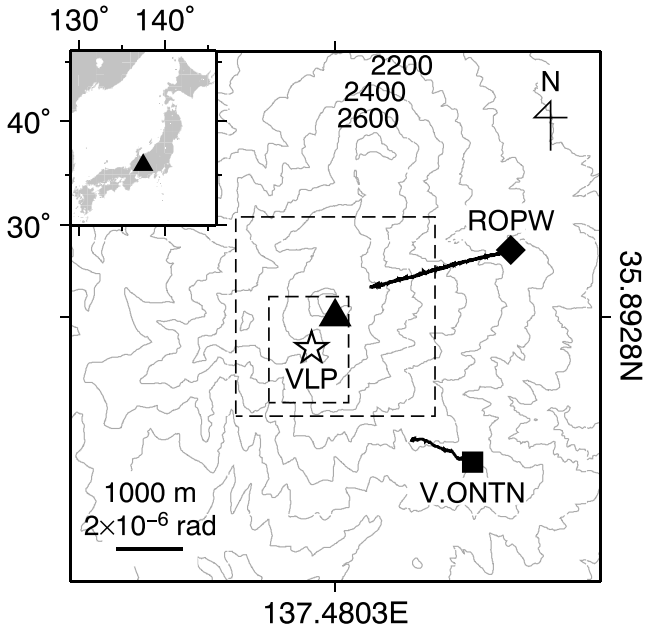

Figure 1. Mount Ontake station network. The square and diamond represent tilt and broadband seismic stations, respectively. Black lines are particle orbits of the tilt waveforms; at ROPW, the seismograms were converted to tilt using the method of *Aoyama and Oshima* [2008]. The triangle and star represent the summit of Mount Ontake and the very long period (VLP) source [*Maeda et al.*, 2015], respectively. Gray lines are topography contours (interval: 200 m). Larger and smaller dashed rectangles represent the map ranges of Figures 3 and 9, respectively. The inset indicates the location of Mount Ontake at a regional scale.

In the present study, we analyzed a tilt change observed immediately before the phreatic eruption of Mount Ontake, Japan, in 2014. We conducted two sets of analyses. One was a waveform inversion, which gave the location and mechanism of the tilt source. The other was a modified phase-space analysis, which independently provided a mathematical expression for the temporal variation in the tilt. Based on the results of these analyses, we constructed simple analytical models for the immediate precursory processes of the 2014 phreatic eruption of Mount Ontake.

2. The Eruption and Precursory Signals of Mount Ontake in 2014

Mount Ontake is the second highest (3067 m) stratovolcano in Japan (inset in Figure 1). Recent activity of the volcano has been characterized by phreatic eruptions in 1979, 1991, and 2007 [*Nakamichi et al.*, 2009]. The 2014 eruption of Mount Ontake started at 11:52:30 local time [*Maeda et al.*, 2015] on 27 September 2014. The eruption produced pyroclastic density current and fallout deposits with a total volume of $0.7-1.3\times10^6$ m^3 [*Maeno et al.*, 2016]. Despite its small size, the eruption resulted in 63 actual and assumed fatalities of people near the crater when it erupted.

The 2014 eruption was preceded by precursory signals with two time scales. One was a swarm of volcano-tectonic (VT) earthquakes that preceded the eruption for approximately 1 month [*Kato et al.*, 2015; *Terakawa et al.*, 2016]. Although a few long-period (LP) events also took place during this period [*Kato et al.*, 2015], the LP activity was considerably lower than that observed before the 2007 eruption [*Nakamichi et al.*, 2009]. The other precursors started approximately 7–10 mins before eruption onset. These precursors consisted of a tremor composed of many VT earthquakes [*Kato et al.*, 2015; *Ogiso et al.*, 2015], very long period (VLP) seismic events [*Maeda et al.*, 2015], and a tilt change (Figure 2a) [*Takagi and Onizawa*, 2016], that were recorded by nearby seismic and tilt stations. Of these precursors, the most difficult to analyze was the tilt change recorded by only one tiltmeter (station V.ONTN; Figure 1). *Takagi and Onizawa* [2016] investigated the volume change of the tilt source but assumed a spherical source at the same location as the source of the inflation in 2007. There has not yet been an investigation of the location, mechanism, and detailed waveform characteristics of the 2014 tilt source.

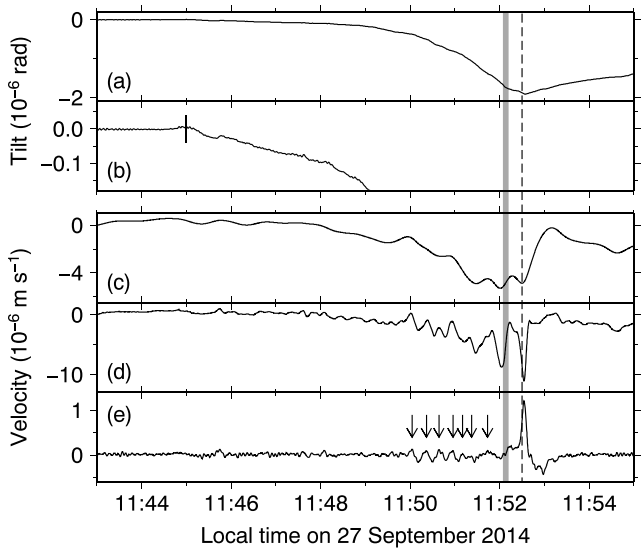

Figure 2. Tilt and velocity records around the time of the eruption onset (11:52:30; the dashed line). (a) The raw EW tilt at V.ONTN. (b) An enlarged plot of Figure 2a. The vertical bar represents an approximate tilt onset time (11:45). (c) The EW velocity at ROPW below 0.02 Hz. (d) The EW velocity at ROPW below 0.1 Hz. (e) The UD velocity at ROPW below 0.1 Hz. The gray bar is the time window of the VLP event analyzed by *Maeda et al.* [2015]. Arrows indicate other VLP events.

The horizontal components of broadband seismometers are well known to be sensitive to tilts, especially below the corner frequencies of the seismometers [*Rodgers*, 1968; *Aoyama and Oshima*, 2008]. At Mount Ontake in 2014, a broadband seismometer was operating at station ROPW in addition to the tiltmeter at V.ONTN (Figure 1). The EW component of the ROPW seismometer, when low-pass filtered at 0.02 Hz (below the corner frequency of the seismometer of 0.033 Hz), showed a transient signal that resembled the tilt change (Figure 2c). This transient signal was also visible in the NS component but not visible in the UD component, suggesting that the transient signal was caused by an instrumental response to the tilt. We then have two stations for analyzing the tilt change in 2014.

The tilt signal in the ROPW record was contaminated by oscillations after 11:50 (Figure 2c). These oscillations were clearer in a higher-frequency band (below 0.1 Hz; Figure 2d for EW and Figure 2e for UD component) and could be interpreted as VLP events. Although most of these VLP events were detectable by the broadband seismometer at ROPW alone, the largest VLP event starting at 11:52:05 was recorded by three additional short-period stations and the source location and mechanism of this event were investigated by *Maeda et al.* [2015].

3. Data Used in the Analyses

In both the waveform inversion and phase-space analyses, we used the tilt record from V.ONTN and broadband seismic record from ROPW (Figure 1). These stations are operated by the Japan Meteorological Agency and Nagano Prefecture, respectively. The tiltmeter at station V.ONTN was mounted in a borehole at a depth of 98 m, and the data were sampled at 1 Hz. The broadband seismometer at station ROPW was a CMG-3T (Guralp Systems Ltd., Aldermaston, Reading, UK) with a natural period of 30 s (Table 1), and the data were sampled at 100 Hz. According to *Maeda et al.* [2015], this seismometer was misoriented by 8° counterclockwise. We corrected for this misorientation in advance for all of the analyses and figures throughout this study. We did not correct for the instrumental response because our analysis method required uncorrected data.

In the waveform inversion, we used a frequency band below 0.02 Hz to suppress contamination from the VLP events (Figure 2). Our data preparation procedure for the waveform inversion was as follows. For each component of the seismic record from ROPW, we applied a two-pole zero-phase Butterworth low-pass filter of 0.02 Hz and then resampled the data at 10 Hz. The sampling rate of 10 Hz was based on a requirement to precisely express the Green functions. For each component of the tilt record from V.ONTN, we first interpolated the data to 10 Hz sampling and then convolved with the tilt response of the ROPW seismometer to simulate a velocity

Table 1. Instrumental Properties of the Broadband Seismometer at ROPW

Parameter	Symbol	Value
Poles	p_1	$-0.02356 + 0.02356i$ Hz
	p_2	$-0.02356 - 0.02356i$ Hz
	p_3	$-50 + 32.2i$ Hz
	p_4	$-50 - 32.2i$ Hz
Zeroes	z_1	$138 + 144i$ Hz
	z_2	$138 - 144i$ Hz
	z_3	0 Hz
	z_4	0 Hz
Constant	A	0.0903

waveform that would have been recorded at V.ONTN if the same seismometer were installed there, and finally applied the same low-pass filter of 0.02 Hz as at ROPW. Here the tilt response of the ROPW seismometer was calculated by multiplying the observed tilt record $\psi(t)$ with the gravitational acceleration g, regarding the resultant $g\psi(t)$ waveform to be equivalent to a ground acceleration, and convolving the seismometer's acceleration response to it (equation (A7)) [*Aoyama and Oshima*, 2008]. We did not apply an instrumental correction for the tiltmeter due to a lack of the instrumental response data. This would not seriously affect the waveform inversion solution below 0.02 Hz as the tiltmeter at V.ONTN was investigated to have a flat response below 0.05 Hz based on our comparison of the Fourier spectra of tilt and broadband seismic records of a distant earthquake. In summary, the data used for the waveform inversion were the three components from ROPW and the two horizontal components from V.ONTN; both were sampled at 10 Hz and included the response of the ROPW seismometer. We used a time window of 11:43–11:55 for the waveform inversion.

In the phase-space analysis, we used first- and second-order integrals of the raw waveforms. Before the integration, we subtracted the average of 11:44–11:45, a period before the appearance of a clear tilt change at 11:45 (Figure 2b), from each trace as the baseline. A possible weak tilt change from 11:44 to 11:45 may have been removed by this operation, but the main tilt change after 11:45 was preserved in the data used for the analysis.

4. Analysis 1: Estimating the Source Location and Mechanism by Waveform Inversion

We performed a joint waveform inversion of the translation and tilt using the method proposed by *Maeda et al.* [2011]. This algorithm is based on the following relationship:

$$V_n(\omega) = M(\omega)\left[G_n^{\mathrm{trans}}(\omega)I_n^{\mathrm{trans}}(\omega) + G_n^{\mathrm{tilt}}(\omega)I_n^{\mathrm{tilt}}(\omega)\right], \quad (1)$$

where ω is the angular frequency, $V_n(\omega)$ is the Fourier transform of the velocity record of nth waveform trace, $M(\omega)$ is the Fourier transform of the source time function, $G_n^{\mathrm{trans}}(\omega)$ and $G_n^{\mathrm{tilt}}(\omega)$ are the Fourier transforms of the Green functions for velocity and tilt rate, respectively, and $I_n^{\mathrm{trans}}(\omega)$ and $I_n^{\mathrm{tilt}}(\omega)$ are the responses of the seismometer to the translation and tilt, respectively. We assumed $I_n^{\mathrm{tilt}}(\omega) = 0$ for the vertical component at ROPW and $I_n^{\mathrm{trans}}(\omega) = 0$ for the simulated velocity records at V.ONTN. For the computation of the Green functions, we used the same finite difference code, topography data, velocity and density structures, grid interval, time stepping, and computational domain as those used in *Maeda et al.* [2015]. We also took into account the borehole depth of V.ONTN.

Since we had only two stations, the degrees of freedom must be reduced to stabilize the waveform inversion solution. To reduce the degrees of freedom, we restricted the search range of the horizontal source location within a narrow (±400 m) region around the VLP source estimated by *Maeda et al.* [2015] (star in Figure 1). We also restricted the source geometry. Crustal deformations at volcanoes are commonly modeled by a spherical [*Mogi*, 1958] or a tensile crack [*Okada*, 1992] source. For the spherical source, the tilt is expected to be axisymmetric [*Mogi*, 1958]. However, the observed tilt pattern was not axisymmetric (Figure 1), so a tensile crack is

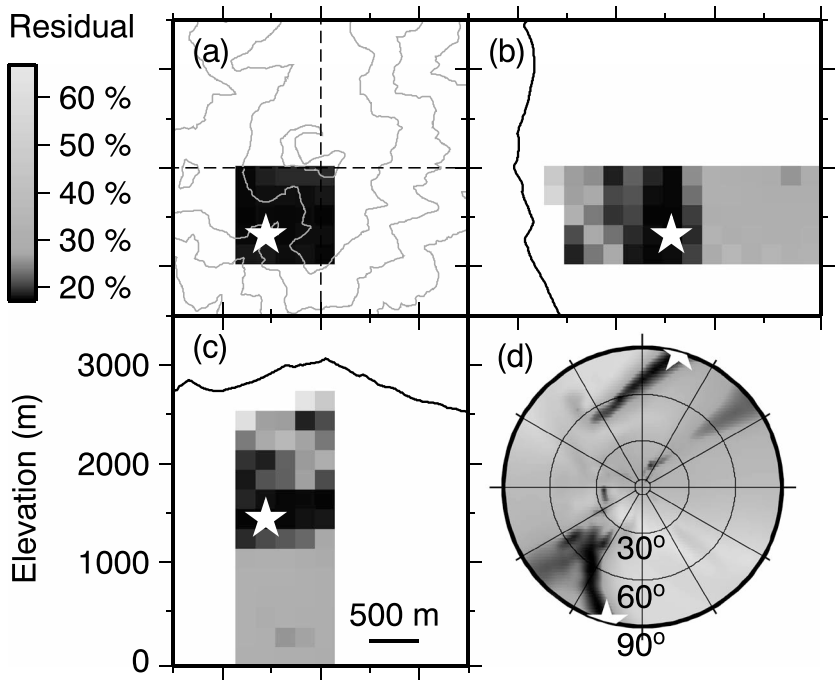

Figure 3. (a–c) A spatial distribution and (d) a crack orientation dependence of the residual between observed and synthetic velocity waveforms. The grid search was conducted for five-parameter combinations, and the result was projected onto each two-parameter plane using the best residual for the other three parameters. The normal vector of the crack is projected onto the upper hemisphere in Figure 3d. Stars represent the best fit solution of the tilt source. Gray lines in Figure 3a are topography contours (interval: 200 m). The map range is shown by the larger dashed rectangle in Figure 1.

the most plausible source mechanism. We assumed a tensile crack source and conducted grid searches for the centroid source location (east, north, and elevation, at 200 m intervals) and orientation (strike and dip at 5° intervals) of the crack. For each grid node, we conducted a frequency-domain waveform inversion of equation (1) to investigate the source time function.

Figure 3 shows the residual between observed and synthetic waveforms plotted against the source location and crack opening direction. The horizontal source location was not well constrained, as is shown by the almost uniform black shade in Figure 3a. In contrast, the vertical source location and crack opening direction were relatively well constrained. Most of the solutions with small ($\leq$ 20%) residuals fell into a source elevation range of 1240–2040 m above sea level (Figures 3b and 3c), suggesting a source depth of around 1000 m beneath the surface. The crack dip angle was constrained within a 45°–90° range (Figure 3d), suggesting that a vertical crack was better than a horizontal crack. The best fit solution with a 17% residual, shown by the stars in Figure 3, was 560 m west and 680 m south of the summit (35.8866°N, 137.4742°E) at 1440 m above sea level having a dip angle of 90° and an opening direction of N15°E. The surface elevation on this best fit solution was 2540 m above sea level, giving a best fit source depth of 1100 m.

The source time function of the moment tensor for the best fit solution showed a moment change of 7.9×10^{15} N m (Figure 4a). Dividing this seismic moment by the rigidity of the elastic medium (6.9×10^9 Pa [*Maeda et al.*, 2015]) gave an estimate of the source volume change of 1.1×10^6 m^3. This volume change is order-of-magnitude consistent with the estimate of *Takagi and Onizawa* [2016] (0.38×10^6 m^3). The observed waveforms were fitted well by synthetic waveforms computed from this best fit source (Figure 4b). We calculated synthetic translation and tilt (Figures 4c and 4d, respectively) and their contributions to the synthetic waveforms. The synthetic waveforms caused by the tilt alone (gray lines in Figure 4e) had larger amplitudes than those caused by the translation alone (black lines in Figure 4e), suggesting that the transient signals were mainly caused by the tilt.

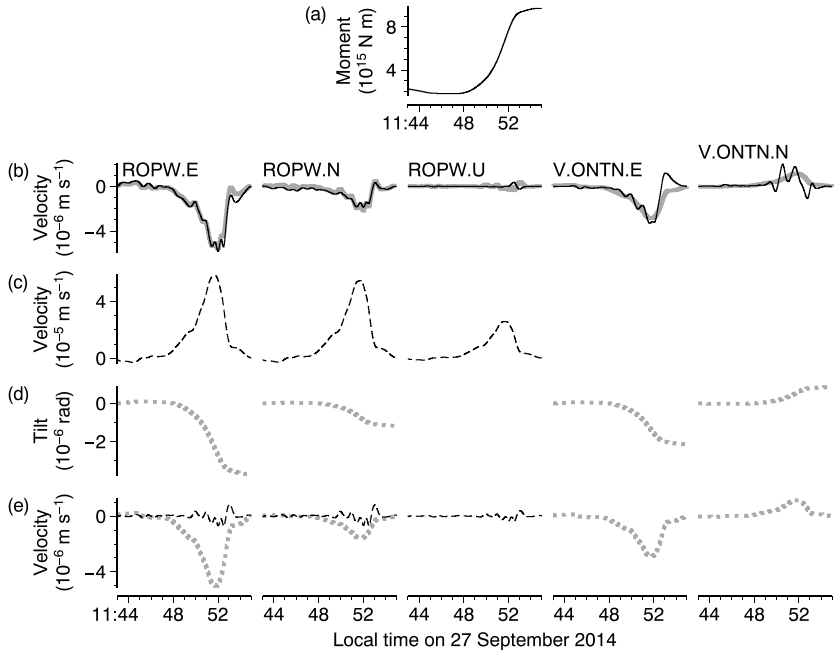

Figure 4. (a) Source time function of the tilt change estimated by waveform inversion. (b) Comparisons of observed (black) and synthetic (gray) waveforms. (c and d) Synthetic ground velocities and tilts caused by the best fit source, computed as the inverse Fourier transforms of $M(\omega)G_n^{\mathrm{trans}}(\omega)$ and $M(\omega)G_n^{\mathrm{tilt}}(\omega)/(i\omega)$ in equation (1), respectively. (e) Synthetic waveforms caused by the translation alone (black) and tilt alone (gray), computed as the inverse Fourier transforms of $M(\omega)G_n^{\mathrm{trans}}(\omega)I_n^{\mathrm{trans}}(\omega)$ and $M(\omega)G_n^{\mathrm{tilt}}(\omega)I_n^{\mathrm{tilt}}(\omega)$, respectively.

5. Analysis 2: Estimating a Mathematical Representation of the Tilt Signal by a Modified Phase-Space

The temporal variation of the tilt before the 2014 eruption of Mount Ontake (Figure 2a) showed an accelerating trend. Similar accelerations have been reported before Strombolian eruptions at Stromboli [*Genco and Ripepe*, 2010], Vulcanian eruptions at Suwanosejima and Semeru [*Iguchi et al.*, 2008], a phreatic eruption at Kuchinoerabujima [*Tameguri et al.*, 2016], and geyser eruptions at Yellowstone [*Vandemeulebrouck et al.*, 2014]. However, the apparent similarity of the waveforms does necessarily point to similar source dynamics because there are many potential models which can explain the accelerating feature of the tilt signals. More detailed characterization of the waveforms is needed to better constrain the source dynamics. In this section, we focus on a mathematical representation of the tilt waveform that would help in understanding the physics of the tilt source process. *Genco and Ripepe* [2010] investigated that the tilt before Strombolian eruptions accelerated at 1.5 power of time, which was the key finding for them to model the source dynamics based on a diffusive gas bubble growth. In case of Mount Ontake, the waveform of the tilt before the 2014 eruption (Figure 2a) resembles an exponential or a power function; however, it is difficult to identify which function is better based on a waveform comparison, as the both functions can explain the waveform almost equally well (Figure 5a). To overcome this difficulty and investigate the best mathematical representation, we made use of the phase-space analysis concept.

A phase-space is a plot of two (or more) time-dependent variables onto a plane as an orbit [e.g., *Braun*, 1993]. Especially useful is an orbit of time series data plotted against its time derivative, from which we may investigate a mathematical representation of the data. Typical phase-space analyses could be explained as the following problem: we have an observed set of time series data $f_k = f(k\Delta t)$ of a time function $f(t)$, but we do not know the mathematical representation of $f(t)$, where k is an integer index and Δt is a sampling interval, and we would investigate the mathematical representation of $f(t)$ using an orbit of f_k versus $(f_k - f_{k-1})/\Delta t$. For example, if the orbit shows an ellipsoidal shape, then we have $f(t)^2/a^2 + \dot{f}(t)^2/b^2 = 1$, which can be arranged as $\ddot{f}(t) = (-b^2/a^2)f(t)$, where a and b are constants, and from which we can investigate that $f(t)$ is a harmonic oscillation. The phase-space has been used for studies of nonlinear oscillations in various fields, including several studies of volcanic tremors [e.g., *Chouet and Shaw*, 1991; *Julian*, 1994; *Konstantinou*, 2002].

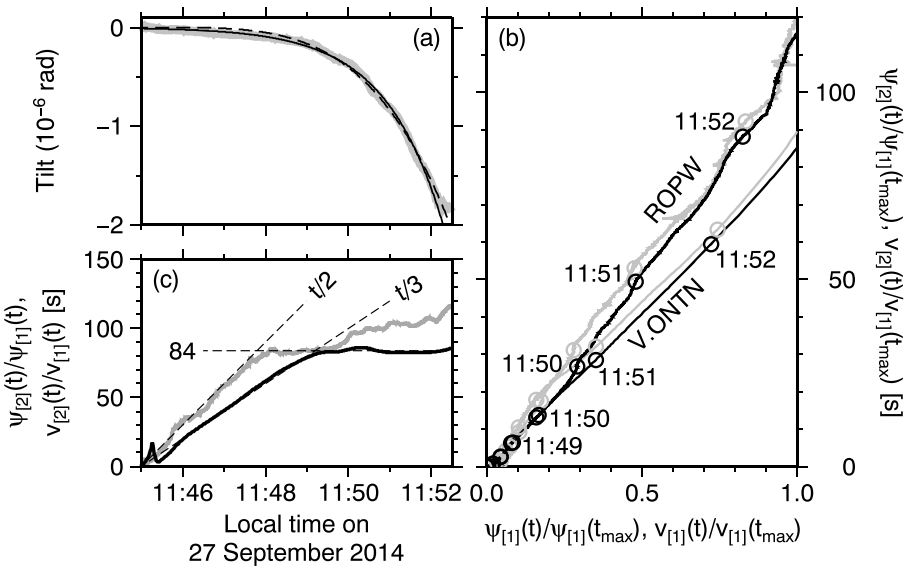

Figure 5. Various plots of the tilt waveforms for investigating the mathematical representation of the temporal variation of the tilt. (a) An EW component of the tilt waveform at V.ONTN (gray). An exponential function -1.1×10^{-8} (rad) $\times \exp(t/\tau)$ and a power function -5×10^{-17} (rad s^{-4}) $\times t^4$, where $\tau = 84$ s and t is time (s) from 11:45, are shown by solid and dashed black lines, respectively. (b) A phase-space plot representing the relationship between first- and second-order integrals of observed waveforms from 11:45:00 to 11:52:30 (t_{max}). The upper and lower two lines are derived from the velocity records at ROPW and the tilt records at V.ONTN, respectively. Black and gray lines are EW and NS components, respectively. Circles represent the data points at every minute. (c) A modified phase-space plot showing the ratios $\psi_{[2]}(t)/\psi_{[1]}(t)$ at V.ONTN (black) and $v_{[2]}(t)/v_{[1]}(t)$ at ROPW (gray) as functions of time. The horizontal vector lengths are used instead of individual components. Dashed lines represent 84 s, $t/2$, and $t/3$.

We applied the phase-space approach to the tilt and velocity records of Mount Ontake. Figure 5b shows the orbits of $(\psi_{[1]}(t), \psi_{[2]}(t))$ at V.ONTN and $(v_{[1]}(t), v_{[2]}(t))$ at ROPW, where t is the elapsed time from 11:45, $\psi(t)$ and $v(t)$ are the tilt and velocity records, respectively (without instrumental corrections), and subscripts [1] and [2] represent first- and second-order integrals, respectively. We used these integrals to amplify the signal of the slow tilt change and to suppress other (higher-frequency) precursory signals. The EW and NS components at each station showed almost the same orbits (Figure 5b), suggesting that the tilt direction was almost constant during the entire period of the analysis. The orbits were nearly straight lines (i.e., $\psi_{[1]}(t) = \dot{\psi}_{[2]}(t) \propto \psi_{[2]}(t)$, $v_{[1]}(t) = \dot{v}_{[2]}(t) \propto v_{[2]}(t)$), suggesting that $\psi(t)$ and $v(t)$ were as first approximation exponential functions. However, the orbits before 11:48, when the signals had small amplitudes, are not clear (Figure 5b).

To see the early part more clearly, we modified the plotting format of the phase-space. Figure 5c shows $\psi_{[2]}(t)/\psi_{[1]}(t)$ and $v_{[2]}(t)/v_{[1]}(t)$ ratios as functions of time. We call this plot a modified phase-space, with the name highlighting that the plot is different in format from the standard phase-space but still focuses on a relationship between a time function and its time derivative. We used horizontal vector lengths of $\psi(t)$ and $v(t)$ in Figure 5c instead of individual components to avoid divisions by small values; this operation is justified by the almost constant tilt direction at each station. We note that the quantities plotted in Figure 5c are different between V.ONTN and ROPW; for V.ONTN, the $\psi_{[2]}(t)/\psi_{[1]}(t)$ ratio calculated from a tilt record is plotted, whereas for ROPW, the $v_{[2]}(t)/v_{[1]}(t)$ ratio calculated from a velocity seismogram is plotted.

We first focus on the $\psi_{[2]}(t)/\psi_{[1]}(t)$ ratio at V.ONTN, which can be simply interpreted in terms of the ground tilt. We note that the integrals $\psi_{[1]}(t)$ and $\psi_{[2]}(t)$ are affected by $\psi(t)$ during the entire period from $t = 0$ to time t. For example, the ratio $\psi_{[2]}(t)/\psi_{[1]}(t)$ at 11:49 is determined by the average behavior of $\psi(t)$ from 11:45 to 11:49 and does not directly reflect the behavior of $\psi(t)$ at 11:49. The integral ratios $\psi_{[2]}(t)/\psi_{[1]}(t)$ at an early time (before 11:48) and a later time (after 11:50) are fitted well by two straight lines (Figure 5c). The earlier part (before 11:48) of the $\psi_{[2]}(t)/\psi_{[1]}(t)$ ratio is fitted well by $\psi_{[2]}(t)/\psi_{[1]}(t) = t/3$, or equivalently

$$\psi_{[1]}(t)/\psi_{[2]}(t) = [d\psi_{[2]}(t)/dt]/\psi_{[2]}(t) = 3/t, \quad (2)$$

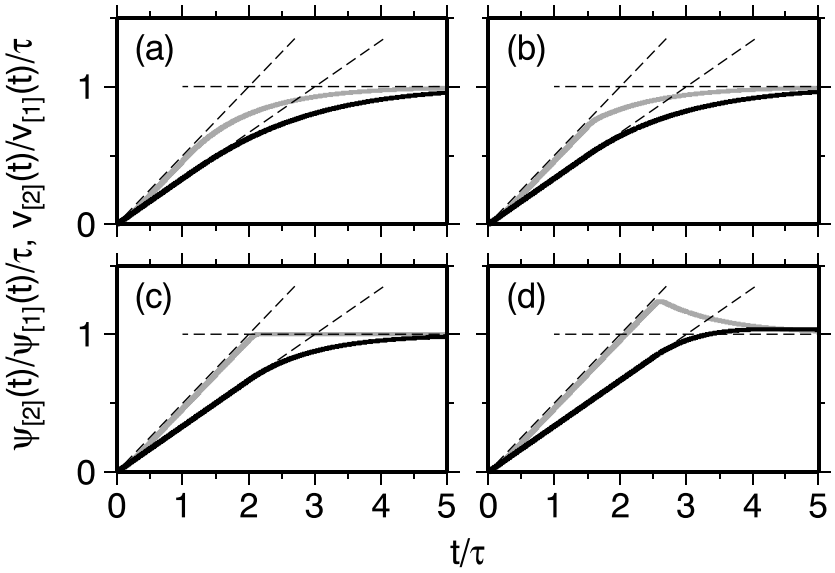

Figure 6. Modified phase-space plots for the synthetic tilt of equation (4). Black and gray lines are the tilt integral ratio $\psi_{[2]}(t)/\psi_{[1]}(t)$ (equation (7)) and the velocity integral ratio $v_{[2]}(t)/v_{[1]}(t)$ (equation (A13)), respectively, with (a) $t_0/\tau = 1$, (b) $t_0/\tau = 3/2$, (c) $t_0/\tau = 2$, and (d) $t_0/\tau = 5/2$. Dashed lines represent τ, $t/2$, and $t/3$.

suggesting that $\psi_{[2]}(t) \propto t^3$, and therefore, $\psi(t) \propto t$. This means that the tilt $\psi(t)$ was initially a linear function of time at least until 11:48. The integral ratio after 11:50 is fitted well by $\psi_{[2]}(t)/\psi_{[1]}(t) = \tau$, or

$$\psi_{[1]}(t)/\psi_{[2]}(t) = [\mathrm{d}\psi_{[2]}(t)/\mathrm{d}t]/\psi_{[2]}(t) = 1/\tau, \tag{3}$$

where $\tau = 84$ s (Figure 5c). The solution of equation (3) is $\psi_{[2]}(t) \propto \exp(t/\tau)$, and therefore, $\psi(t) \propto \exp(t/\tau)$. This observation could be interpreted as follows: at a certain moment of time before 11:50, the tilt $\psi(t)$ switched to exponential growth, and the effect of this exponential growth became dominant in the integral ratio after 11:50. We could then interpret that the tilt $\psi(t)$ at V.ONTN first increased linearly with time, then switched to exponential growth. This temporal variation of the tilt is expressed as

$$\psi(t) = \begin{cases} 0 & (t \le 0) \\ \psi_0 t/t_0 & (0 < t \le t_0) \\ \psi_0 \exp[(t-t_0)/\tau] & (t_0 < t \le t_{\max}) \end{cases}, \tag{4}$$

where t_0 is time of the transition from the linear to exponential regime, ψ_0 is the tilt at $t = t_0$, $t_{\max}$ is the time of the eruption onset (11:52:30), and the tilt change is assumed to have started at 11:45 ($t = 0$) (Figure 2b).

An interpretation of the $v_{[2]}(t)/v_{[1]}(t)$ ratio at ROPW is more complicated in that the data for this plot consist of the instrumental response of the seismometer to a mixed input of the ground translation and tilt. Apparently, the $v_{[2]}(t)/v_{[1]}(t)$ ratio looks well fitted by $v_{[2]}(t)/v_{[1]}(t) = t/2$ for 11:45–11:48 and $v_{[2]}(t)/v_{[1]}(t) = \tau$ for 11:48–11:50 (Figure 5c). After 11:50, repeated VLP events may have contaminated the tilt signal (Figure 2), so we focus on a period before 11:50 for characterizing the tilt signal at ROPW.

We now show that the $\psi_{[2]}(t)/\psi_{[1]}(t)$ ratio at V.ONTN and $v_{[2]}(t)/v_{[1]}(t)$ ratio at ROPW (before 11:50) can be consistently explained by the same tilt of equation (4). Indeed, integrating equation (4) with time yields

$$\psi_{[1]}(t) = \begin{cases} 0 & (t \le 0) \\ \psi_0 t^2/(2t_0) & (0 < t \le t_0) \\ \psi_0(t_0/2 - \tau) + \psi_0 \tau \exp[(t-t_0)/\tau] & (t_0 < t \le t_{\max}) \end{cases}, \tag{5}$$

$$\psi_{[2]}(t) = \begin{cases} 0 & (t \le 0) \\ \psi_0 t^3/(6t_0) & (0 < t \le t_0) \\ \psi_0(t_0^2/6 - \tau^2) + \psi_0(t_0/2 - \tau)(t - t_0) & \\ \quad + \psi_0 \tau^2 \exp[(t-t_0)/\tau] & (t_0 < t \le t_{\max}) \end{cases}, \tag{6}$$

and therefore,

$$\psi_{[2]}(t)/\psi_{[1]}(t) = \begin{cases} t/3 & (0 < t \le t_0) \\ \tau + \{(t_0/2)(t_0/3 - \tau) + (t_0/2 - \tau)(t - t_0)\}/ & \\ \{t_0/2 - \tau + \tau \exp[(t - t_0)/\tau]\} & (t_0 < t \le t_{\max}) \end{cases}. \quad (7)$$

A theoretical $v_{[2]}(t)/v_{[1]}(t)$ formula for the ground tilt of equation (4) is derived in Appendix A (equation (A13)). In Figure 6, we plot equations (7) and (A13) for several values of t_0/τ. The sharp bending of $v_{[2]}(t)/v_{[1]}(t)$ observed around the time when the ratio reaches the constant value (gray line in Figure 5c) is reproduced by the formula only when t_0/τ is around 2 (Figure 6c). For example, if we assume $t_0/\tau = 3/2$, the slope of $v_{[2]}(t)/v_{[1]}(t)$ gradually decreases from 1/2 to zero (Figure 6b), which is not consistent with the observation that the slope abruptly changed from 1/2 to zero (Figure 5c). If we assume $t_0/\tau = 5/2$, the $v_{[2]}(t)/v_{[1]}(t)$ ratio overshoots at the transition (Figure 6d), which is not consistent with the observation. In the following, we use $\tau = 84$ s and $t_0/\tau = 2$ as representative values. Using these values, the theoretical $\psi_{[2]}(t)/\psi_{[1]}(t)$ formula closely matched the observed curve of $\psi_{[2]}(t)/\psi_{[1]}(t)$ at V.ONTN (Figure 7a) and the same argument held for $v_{[2]}(t)/v_{[1]}(t)$ at ROPW (Figure 7b). This indicates that the tilt record at V.ONTN and velocity record at ROPW are consistently explained by the common tilt represented by equation (4).

As was mentioned earlier, it is difficult to determine whether an exponential or power function is better based on fits to the original record (Figure 5a). However, using the phase-space, appropriateness of these functions can be easily evaluated. In Figure 7c, we plot synthetic $\psi_2(t)/\psi_1(t)$ ratios for a power function

$$\psi(t) = at^b, \psi_{[2]}(t)/\psi_{[1]}(t) = t/(b+2), \quad (8)$$

where a and b are constants, showing clear discrepancies from the data. We can therefore conclude that the exponential function explains the data better than the power function.

Since the wavelength of the tilt signal is substantially longer than the distances between the source and receivers, we assume that the source volume change is described by the same formula as equation (4):

$$\Delta V(t) = \begin{cases} 0 & (t \le 0) \\ \Delta V_0 t/t_0 & (0 < t \le t_0) \\ \Delta V_0 \exp[(t - t_0)/\tau] & (t_0 < t \le t_{\max}) \end{cases}, \quad (9)$$

where ΔV_0 is a constant. Differentiating equation (9) with time yields

$$\Delta \dot{V}(t) = \begin{cases} 0 & (t \le 0) \\ \Delta V_0/t_0 & (0 < t \le t_0) \\ \Delta V_0 \exp[(t - t_0)/\tau]/\tau & (t_0 < t \le t_{\max}) \end{cases}. \quad (10)$$

The final source volume expected from equation (9) is $\Delta V(t_{\max}) = \Delta V_0 \exp[(t_{\max} - t_0)/\tau]$. Assuming that this final source volume is equal to that estimated by the waveform inversion (i.e., $\Delta V(t_{\max}) = 1.1 \times 10^6$ m^3), we have $\Delta V_0 = 3.8 \times 10^4$ m^3, and $\Delta \dot{V}(t) = \Delta V_0/t_0 = 2.3 \times 10^2$ m^3 s^{-1} for $0 < t \le t_0$.

6. Discussion

A difficulty in modeling the tilt source of the Mount Ontake 2014 eruption is that only two stations were available. This limitation especially affects the reliability of the source location and mechanism estimated by the waveform inversion. In contrast, the phase-space analysis could be conducted trace by trace, so that our interpretation of the linear and exponential time functions based on the phase-space analysis is considered reliable regardless of the small number of stations. Taking these aspects into account, our discussion below will focus on explaining these time functions using simple analytical models.

6.1. Assumptions

We assume that the volume change of the tilt source was caused by the boiling of underground water at constant pressure and temperature. This assumption is based on the following reasoning. Since a gas phase can expand far more easily than solid and liquid phases and water vapor occupies more than 90% mole fraction of volcanic gases in most fields [*Fischer*, 2008], it is reasonable to assume that the volume change of water vapor

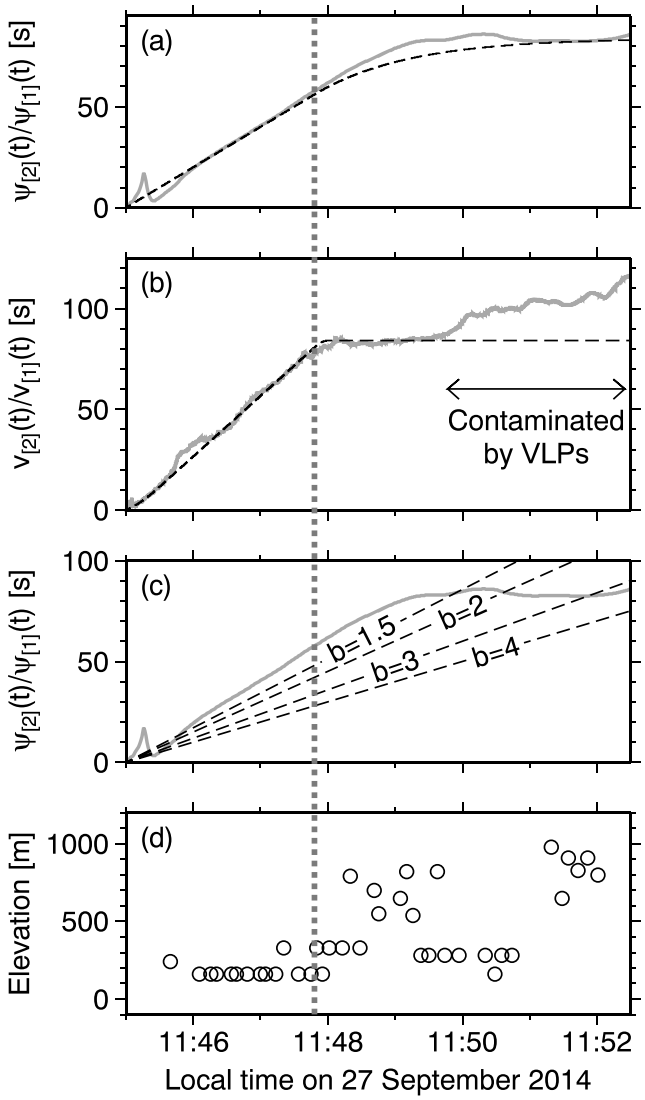

Figure 7. Comparisons of observed and synthetic modified phase-space plots. Gray curves are (a) the observed $\psi_{[2]}(t)/\psi_{[1]}(t)$ ratio at V.ONTN and (b) the observed $v_{[2]}(t)/v_{[1]}(t)$ ratio at ROPW. Dashed curves are synthetic $\psi_{[2]}(t)/\psi_{[1]}(t)$ and $v_{[2]}(t)/v_{[1]}(t)$ ratios (equations (7) and (A13)) for $\tau = 84$ s and $t_0 = 2\tau = 168$ s. (c) A comparison of the observed $\psi_{[2]}(t)/\psi_{[1]}(t)$ ratio at V.ONTN (gray) and synthetic ratios for power functions with various b (dashed lines; equation (8)). (d) Hypocenter elevations of VT earthquakes [*Kato et al.*, 2015]. The vertical line represents the estimated time of the transition from linear to exponential ($t_0 = 2\tau = 168$ s).

was the primary cause of the tilt change before the eruption of Mount Ontake in 2014. Since the eruption was phreatic, the temperature of the water vapor is considered to be relatively low, near the boiling point. For an existing temperature estimate, we may refer to *Ikehata and Maruoka* [2016], who investigated the source temperature of the sulfur erupted in 2014 to be 543–554 K. At such low temperatures, an ideal gas is not a good approximation, as shown later. Instead of the ideal gas, we use the most reliable existing equation of state of liquid water and water vapor, known as IAPWS-95 [*Wagner and Pruss*, 2002], developed by the International Association for the Properties of Water and Steam (IAPWS). In IAPWS-95, the pressure of water vapor is given by a 56-term noninteger polynomial of the temperature and volume. Given this very complicated relationship involving pressure, temperature, and volume, it is practically impossible to realize the observed simple linear and exponential time functions of the volume change by considering any physical processes as long as temporal variations of pressure and temperature are allowed. For this reason, the pressure and temperature have to be considered as constants; then boiling of liquid water is the only process to realize the volume change of the water vapor.

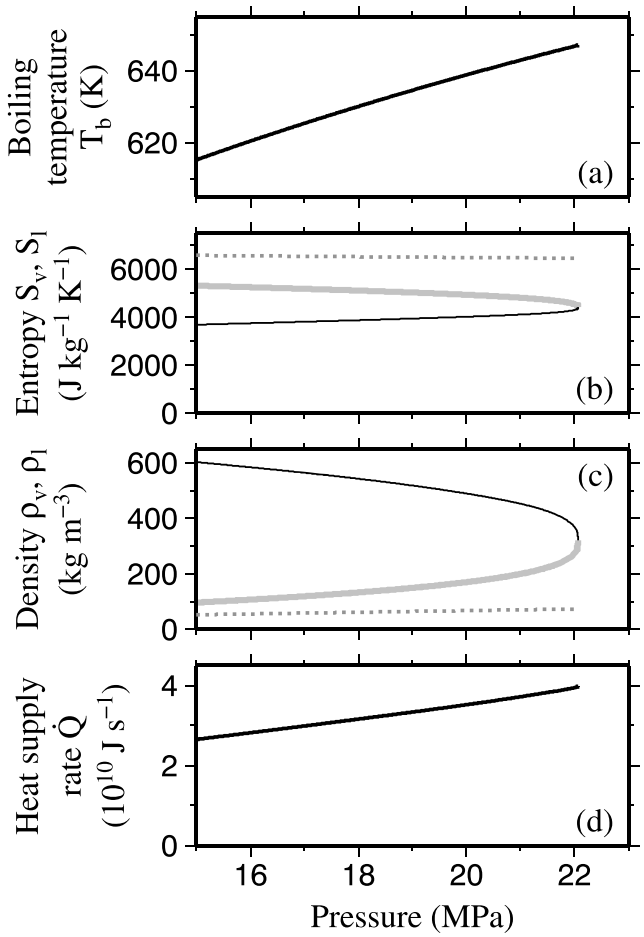

Figure 8. (a) Boiling temperature of water plotted against pressure. (b) Entropies and (c) densities of liquid water (black) and water vapor (gray) at the boiling temperature. Solid and dotted lines are calculated with IAPWS-95 [*Wagner and Pruss*, 2002] and the ideal gas, respectively. For the ideal gas, the entropy is given only as a relative value in the thermodynamics, and we used equation (5.63) of *Greiner et al.* [1995] in the statistical mechanics to determine the absolute value. (d) The heat supply rate $\dot{Q}$ calculated with equation (14) and IAPWS-95.

In Figures 8b and 8c, we compare the entropies and densities, respectively, of water vapor at the boiling temperature of each pressure computed by the ideal gas and IAPWS-95. The two equations of state show large discrepancies, indicating that the ideal gas is not a good approximation at low temperatures.

The requirement of constant pressure implies that the tilt source did not move vertically during the tilt change; the vertical movement of the source depth would result in a temporal variation of the ambient lithostatic pressure. In reality, we consider that some fraction of the water vapor may have migrated upward, but either the mass or distance of the migration was small enough to ignore its contribution to the total volume change. We also note that a constant depth is required during the linear stage and during the exponential stage individually, but a depth change is allowed at the time of the transition.

In agreement with most modeling studies in volcanology, we assume that the pressure at the source depth is near that of lithostatic load. The best fit source depth of the waveform inversion solution (1100 m) corresponds to a lithostatic pressure of 25 MPa if we assume a density of 2300 kg m^{-3} (the value used in the waveform inversion). However, boiling of liquid water can occur only below the critical point of 22.064 MPa [*Wagner and Pruss*, 2002]; above this pressure, a second-order phase transition of water from liquid to supercritical state can occur, but this does not involve a volume change. We may consider two scenarios to realize the boiling at the source depth. One is to consider an uncertainty of the source depth. The source depth has an uncertainty of at least ±200 m (Figures 3b and 3c). For example, the residual at a location 200 m above the best fit solution (17.8%) is almost the same as that of the best fit solution (17.3%). Taking into account this uncertainty and

considering a source depth of 900 m, the corresponding lithostatic pressure is 20 MPa, which is below the critical point. Another candidate explanation is that the real volcanic gas is not pure water vapor. According to *Gallagher et al.* [1993], the critical pressure would rise to 26.79 MPa if only 3.5 mol % of CO_2 contaminates the water vapor. Since the contamination of 3.5 mol % of CO_2 is possible at volcanoes [*Fischer*, 2008], the boiling of water at 25 MPa could occur. Although this may be a realistic scenario, our calculations below will use pure water at pressures lower than 22.064 MPa, which is the only possible way of quantitative discussion given the lack of gas composition data at Mount Ontake. We consider a relatively wide pressure range of 15–22.063 MPa to take into account an uncertainty of the source pressure on our model. Since we consider the boiling, we assume the temperature to be at the boiling point for each assumed pressure. Depending on the pressure, the boiling temperature used in the model ranged from 615 K to 647 K (Figure 8a).

6.2. Model of the Linear Time Function of the Tilt

The linear function of time during the early period of the tilt change could be explained by boiling of underground water controlled by constant heat supply from a greater depth. Let $\dot{Q}$ be the heat supply rate, $\dot{m}$ be the mass of water that boiled during a unit time, and Q_l be the latent heat of water per unit mass. An energy balance between the supplied heat and the heat consumed by the boiling is

$$\dot{Q} = \dot{m} Q_l. \tag{11}$$

The latent heat is given by

$$Q_l = T_b(S_v - S_l), \tag{12}$$

where T_b is the boiling temperature of water and S_l and S_v are entropies of liquid water and water vapor at T_b, respectively. The volume change rate $\Delta\dot{V}$ caused by the boiling is

$$\Delta\dot{V} = \dot{m}/\rho_v - \dot{m}/\rho_l = \dot{m}(\rho_l - \rho_v)/\rho_v\rho_l, \tag{13}$$

where ρ_l and ρ_v are densities of liquid water and water vapor at T_b, respectively. Equations (11)–(13) yield

$$\dot{Q} = [\rho_v\rho_l T_b(S_v - S_l)/(\rho_l - \rho_v)]\Delta\dot{V}. \tag{14}$$

Using $\Delta\dot{V} = 2.3 \times 10^2$ m^3 s^{-1} estimated in the previous section, we obtain $\dot{Q} = 2.7$–4.0×10^{10} J s^{-1} for the pressure range of 15–22.063 MPa (Figure 8d). This heat supply rate is in order of magnitude consistent with the surface heat emission of 5.2×10^9 J s^{-1} estimated by the plume on 28 September 2014 (the day after the eruption) [*Terada*, 2014].

6.3. Model of Exponential Tilt Growth

Boiling can occur due to heating and depressurization. Since the linear function was explained by the heating, it is natural to expect the exponential time function to have been caused by boiling due to depressurization. However, constant pressure is needed to realize the exponential function, as was mentioned in section 6.1. To realize the decompression-induced boiling under constant pressure, we consider the following scenario: the expansion of water vapor results in a decrease in the gas pressure at the boiling depth that is immediately compensated by additional boiling of water to keep the pressure constant. We consider a positive feedback in this scenario such that the greater the water vapor volume, the faster the expansion, resulting in more rapid boiling. An exponential time function is realized if the expansion rate is proportional to the water vapor volume.

To model the expansion process, we consider a buoyancy-driven vertical Darcy flow of water vapor through a permeable region of many small subparallel cracks (Figure 9a). If we consider a laminar flow in a single large tensile crack filled with water vapor, then the buoyancy force is large and the resistant viscous force of water vapor is small, resulting in a fast upward migration of water vapor. This is inconsistent with the relatively long duration of 450 s of the tilt change; water vapor has to be kept underground for 450 s without reaching the surface from a depth of 1100 m. In the case of the Darcy flow, the narrow passages enable the resistant viscous force to act efficiently, thereby realizing a slow migration of water vapor. We regard the waveform inversion solution as an average of the openings of the small cracks.

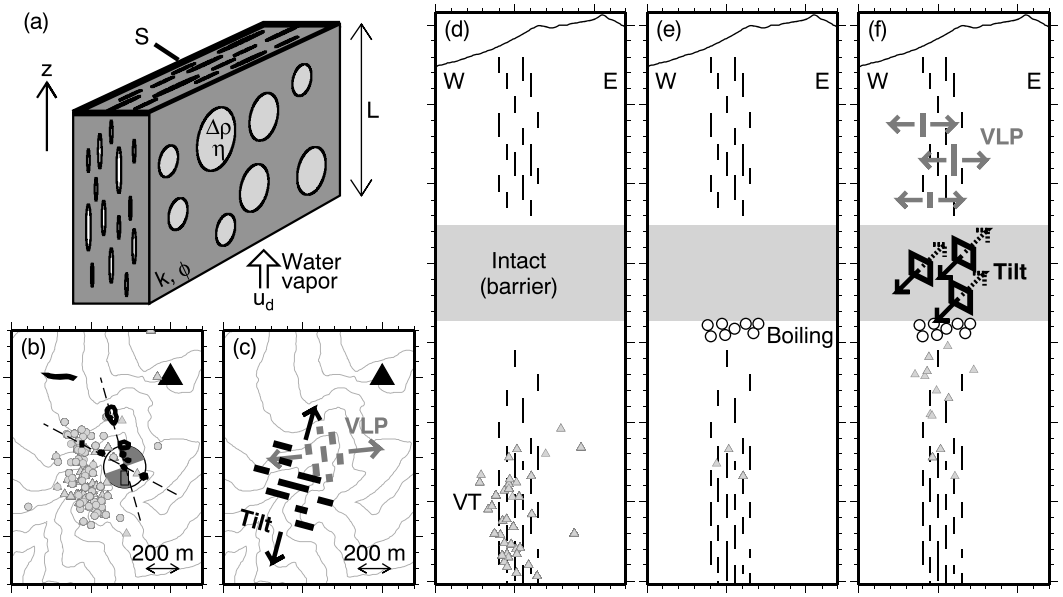

Figure 9. Interpretation of the precursory processes. (a) Conceptual model of the exponential time function. The source volume change is given by $\Delta V(t) = SL\phi(t)$. (b) Comparison of the VT hypocenters before (triangles) and after (circles) the eruption as estimated by *Kato et al.* [2015], the regional stress field estimated by *Terakawa et al.* [2016] (the focal sphere), and eruptive vent locations estimated by the Geospatial Information Authority of Japan (bold outlines; http: //www.gsi.go.jp/BOUSAI/h26-ontake-index.html, accessed 9 June 2015). Two dashed lines show NNW-SSE and WNW-ESE trends of the eruptive vent locations. The black triangle and gray thin lines are the summit of Mount Ontake and topography contours (interval: 100 m), respectively. The map range is the smaller dashed rectangle in Figure 1. (c) Schematic illustrations of the VLP [*Maeda et al.*, 2015] and tilt sources on a horizontal map. The crack orientations are based on the best fit waveform inversion solutions. (d–f) Schematic interpretations of the precursory processes on a vertical section during the long-term precursory stage (before 11:45), the linear tilt change (11:45–11:48), and the exponential tilt growth (11:48–11:52:30), respectively. The earthquakes in each time period detected by a matched filter analysis [*Kato et al.*, 2015] are plotted. Vertical lines and white circles represent preexisting seismic faults and bubbles of water vapor, respectively.

The Darcy flow through a permeable region of the small cracks is modeled as follows. For simplicity, we consider a rectangular region with a vertical length L and a cross-sectional area S occupied by the small cracks (Figure 9a). The Darcy velocity u_d of the buoyancy-driven flow is given as [*Turcotte and Schubert*, 2002]

$$u_d = k\Delta\rho g/\eta, \tag{15}$$

where k is the vertical permeability of the system, $\Delta\rho$ is the density difference between the surrounding solid medium and water vapor, g is the gravitational acceleration, and η is the viscosity of water vapor. Among the quantities in the right side of equation (15), $\Delta\rho$, g, and η cannot vary significantly with time, whereas k can vary with time through an evolution of the porosity

$$\phi(t) = \Delta V(t)/(SL). \tag{16}$$

We here assume zero initial volume of water vapor (i.e., $\Delta V(t) = V(t)$) and ignore isolated, empty pores that have only minor effects on the permeability; the permeability is mainly controlled by interconnected pores, and such pores are easily filled with injected fluids. There is no one-to-one relationship between the porosity and permeability, but classical models suggest that

$$k(t) = k_0\phi(t)^n, \tag{17}$$

where k_0 and n are positive constants [e.g., *Bernabe et al.*, 2003]. The upward volumetric flux of water vapor is given by $Su_d(t)$. In our model, this upward migration of water vapor is compensated by boiling of water at a rate $\Delta\dot{V}(t)$, suggesting that

$$\Delta\dot{V}(t) = Su_d(t). \tag{18}$$

Equations (15) to (18) yield

$$\Delta\dot{V}(t) = (Sk_0\Delta\rho g/\eta)[\Delta V(t)/(SL)]^n. \quad (19)$$

Equation (19) shows that the exponential tilt growth is realized if $n = 1$. Since Darcy's law represents an average of laminar flows through many small channels, the permeability is proportional to the product of the number density of the channels by the square of the individual channel widths [*Turcotte and Schubert*, 2002]. Based on this theoretical aspect, $n = 2$ is expected if the porosity increase results from extensions of individual channel widths, whereas $n = 1$ is expected if the porosity increase is caused by an increase of the number density of the channels. Consequently, the exponential growth of the source volume is explained by an increase of the number density of small cracks.

In the case of $n = 1$, equation (19) is rewritten as

$$\Delta\dot{V}(t) = [(\Delta\rho g k_0)/(\eta L)]\Delta V(t). \quad (20)$$

This equation can be compared with equations (9) and (10) to obtain the time constant τ of the exponential growth as

$$1/\tau = (\Delta\rho g k_0)/(\eta L). \quad (21)$$

From equations (17) and (21), we have

$$k(t) = (\eta L)/(\Delta\rho g\tau)\phi(t). \quad (22)$$

Assuming $\Delta\rho = 2000$ kg m^{-3}, $g = 9.8$ m s^{-2}, $\eta = (2.3–4.7)\times10^{-5}$ Pa s (at the boiling temperatures at 15–22.063 MPa) [*Wagner and Pruss*, 2002], and using the observed τ value of 84 s, we obtain $k(t)$ (m^2) = $(1.4–2.8)\times10^{-11}$ (m) $\times L$ (m) $\times \phi(t)$. The vertical length scale of the source volume L (Figure 9a) must be sufficiently smaller than the source depth scale to keep the pressure change small. The value of $k(t)$ is proportional to those of L and $\phi(t)$, and in case of $L = 100$ m and $\phi(t) = 0.1$ (10% porosity), for example, we obtain $k(t) = (1.4–2.8)\times10^{-10}$ m^2. This permeability is near that of sand [*Turcotte and Schubert*, 2002], suggesting that the value is not unrealistic in natural fields. We note that this permeability is near the upper limit reached during the later period of intense cracking; initially, the porosity due to the cracks, and therefore the permeability, is likely to have been considerably smaller.

6.4. Summary of the Precursory Processes

Figure 9 summarizes our interpretation for the precursors of the 2014 eruption and comparisons with the results of several previous studies. Hypocenters of VT earthquakes showed an NNW-SSE trend [*Kato et al.*, 2015], which is subparallel to one of the maximum shear directions in the regional stress field [*Terakawa et al.*, 2016] (Figure 9b). According to *Terakawa et al.* [2016], focal mechanisms of the VT earthquakes changed to an ENE-WSW tension before the eruption. These results were explained by the injection of fluids into preexisting seismic faults along the NNW-SSE trend. *Maeda et al.* [2015] made an interpretation that the source mechanism of the largest VLP event starting at 11:52:05 was an ENE-WSW opening (NNW-SSE striking) subvertical tensile crack. They interpreted this source as one of the NNW-SSE trending preexisting seismic faults that opened due to inflow of ascending gas. Repeated occurrences of VLP events after 11:50 (Figure 2) suggest that similar opening events of the preexisting faults may have repeatedly taken place (Figure 9c). In summary, both VT and VLP events were probably caused by injection of volcanic fluids into preexisting seismic faults.

In contrast, the tilt change is most likely to have been caused by newly created cracks in an intact region, i.e., a region with no or very few preexisting cracks. As was discussed in the previous section, the exponential time function of the tilt change was explained by a permeable flow model with $n = 1$ (equation (19)), suggesting that the source volume change was controlled by an increase in the number density of small cracks and not by extensions of individual crack thicknesses. The increase in the number density of small cracks is more consistent with the breakage of an intact region than openings of preexisting seismic faults. Based on this idea, we consider the following scenario: there was an intact region that had acted as a permeability barrier for upward migration of fluids during the month before the eruption (Figure 9d), and a breakage of this barrier due to intense boiling during the immediate precursory period led to the eruption (Figures 9e and 9f). Such a barrier would be a reasonable assumption for a phreatic eruption model. A sealed structure is needed to

realize a phreatic eruption [e.g., *Christenson et al.*, 2010; *Maeno et al.*, 2016]; if the sealed structure had been absent, water vapor would have easily escaped from the ground as a gentle degassing and not as an explosion. Immediately beneath the sealed structure, mass and heat transported from a greater depth by volcanic fluids may have easily accumulated, which may have facilitated the occurrence of the phreatic eruption.

This conceptual model is consistent with the occurrence of an intense VT swarm, which is an indicator of brittle failure, during the period of the tilt change. *Kato et al.* [2015] investigated the VT hypocenters and pointed out that the hypocenters moved upward before the eruption. In Figure 7d, we show a vertical time section of the VT hypocenters determined by *Kato et al.* [2015]. The hypocenters moved to shallower depths at around 11:48, near the time of the transition from linear to exponential tilt growth. This suggests that the cracking of the intact region began at around 11:48; before 11:48, accumulation of water vapor immediately beneath the intact region may have caused the linear tilt change and deeper VT earthquakes (Figure 9e). The barrier may have enabled a slow migration of water vapor, consistent with the requirement of a constant pressure. Although a small volume of water vapor may have passed through the barrier region and traveled further upward to generate the VLP events after 11:50 (Figure 9f), this does not affect the entire behavior of the tilt change; the volume of the water vapor involved in the VLP events (75 m^3 for the largest VLP event) [*Maeda et al.*, 2015] is 4 orders of magnitude smaller than that involved in the tilt change.

The eruptive vent locations showed two trends, one NNW-SSE and the other WNW-ESE (Figure 9b). The NNW-SSE trend can be explained by upward migration of fluids through the preexisting seismic faults, whereas no explanation has been proposed for the WNW-ESE trend. The best fit tilt source was WNW-ESE striking (NNE-SSW opening), subparallel to the unexplained trend of the eruptive vents (Figure 9c). Although the waveform inversion solution has some uncertainty due to the small number of stations, one candidate's simultaneous explanation for the best fit tilt source and eruptive vent trend may be that the local stress was NNE-SSW tension at a very shallow depth (around 1000 m or less; shallower than the VT source depths) beneath the eruptive vent region. We note that NNE-SSW was the tension direction in the regional stress field (Figure 9b), although we are not sure whether it was the regional stress or more local shallow effects that controlled the tilt source and vent trend.

7. Conclusions

We analyzed a tilt change recorded at Mount Ontake during the 450 s immediately prior to the onset of the 2014 phreatic eruption. Our waveform inversion of the tilt change using a tilt record and a broadband seismic record pointed to a vertical tensile crack at a depth of 1100 m that opened by a volume of 1.1×10^6 m^3. To characterize the waveforms of the tilt signals, we calculated the temporal evolution of second-order to first-order integral ratios for both records (modified phase-spaces). This analysis showed that the tilt changes at the two stations were consistent with a linear time function followed by exponential growth. The linear function was explained by the boiling of underground water under a constant heat supply from a greater depth. To explain the exponential function, we assumed the tilt source to be a region occupied by many small cracks filled with water vapor and modeled this system as a vertical flow through a permeable medium. We considered the temporal evolution of the permeability due to increasing water vapor volume controlled by decompression-induced boiling. According to this model, exponential growth is realized if the permeability is proportional to the porosity; this requirement is satisfied if the porosity increase is due to an increase of the number density of cracks, rather than expansions of individual cracks, suggesting that the tilt change was caused by cracking of a previously intact region. This region may have acted as a permeability barrier for upward fluid migration prior to the start of the tilt change, and breaking the barrier may have led to the eruption.

Appendix A: Synthetic Velocity Record at ROPW Caused by a Tilt of Equation (4)

The instrumental response of a seismometer to tilt is usually computed numerically. However, the numerical convolution is unstable when a large jump exists between the initial and final values of the input signal, which is the case in equation (4). To avoid this instability, we derived an analytical expression for the synthetic horizontal velocity record at ROPW caused by a tilt of equation (4). Using the instrumental parameters in Table 1,

the response of the broadband seismometer at ROPW to a unit velocity impulse is expressed in the frequency domain as

$$\begin{aligned} I_v(\omega) &= \frac{A(i\omega)^2(i\omega - 2\pi z_1)(i\omega - 2\pi z_2)}{(i\omega - 2\pi p_1)(i\omega - 2\pi p_2)(i\omega - 2\pi p_3)(i\omega - 2\pi p_4)} \\ &= \frac{A\omega^2(\omega + 2\pi i z_1)(\omega + 2\pi i z_2)}{(\omega + 2\pi i p_1)(\omega + 2\pi i p_2)(\omega + 2\pi i p_3)(\omega + 2\pi i p_4)}, \end{aligned} \tag{A1}$$

where ω is the angular frequency. The response of this seismometer to a unit acceleration impulse at $t = 0$ is represented in the time domain as

$$\begin{aligned} i_a(t) &= [1/(2\pi)] \int_{\infty}^{\infty} \mathrm{d}\omega \exp(i\omega t)[I_v(\omega)/(i\omega)] \\ &= [1/(2\pi i)] \int_{\infty}^{\infty} \mathrm{d}\omega \exp(i\omega t) \\ &\quad \frac{A\omega(\omega + 2\pi i z_1)(\omega + 2\pi i z_2)}{(\omega + 2\pi i p_1)(\omega + 2\pi i p_2)(\omega + 2\pi i p_3)(\omega + 2\pi i p_4)} \\ &= \begin{cases} 0 & (t \le 0) \\ \sum_{n=1}^{4} c_n \exp(2\pi p_n t) & (t > 0) \end{cases}, \end{aligned} \tag{A2}$$

where

$$c_1 = Ap_1(p_1 - z_1)(p_1 - z_2)/[(p_1 - p_2)(p_1 - p_3)(p_1 - p_4)], \tag{A3}$$

$$c_2 = Ap_2(p_2 - z_1)(p_2 - z_2)/[(p_2 - p_1)(p_2 - p_3)(p_2 - p_4)], \tag{A4}$$

$$c_3 = Ap_3(p_3 - z_1)(p_3 - z_2)/[(p_3 - p_1)(p_3 - p_2)(p_3 - p_4)], \tag{A5}$$

and

$$c_4 = Ap_4(p_4 - z_1)(p_4 - z_2)/[(p_4 - p_1)(p_4 - p_2)(p_4 - p_3)]. \tag{A6}$$

For a horizontal component of the seismometer, a ground tilt $\psi(t)$ is equivalent to a ground acceleration $g \sin\psi(t) \sim g\psi(t)$ [*Rodgers*, 1968]. Thus, the seismic record expected to be observed due to the tilt is

$$v(t) = g \int_{-\infty}^{\infty} \psi(t') i_a(t - t') \mathrm{d}t'. \tag{A7}$$

Inserting equations (4) and (A2) into (A7) yields

$$v(t) = \begin{cases} 0 & (t \le 0) \\ \psi_0 g \sum_{n=1}^{4} C_{1n}[\exp(2\pi p_n t) - 1] & (0 < t \le t_0) \\ \psi_0 g \sum_{n=1}^{4} \left\{ C_{1n} \exp[2\pi p_n t] - C_{2n} \exp[2\pi p_n (t - t_0)] \right. & \\ \left. + C_{3n} \exp[(t - t_0)/\tau] \right\} & (t_0 < t \le t_{\max}) \end{cases}, \tag{A8}$$

where

$$C_{1n} = c_n/(4\pi^2 p_n^2 t_0), \tag{A9}$$

$$C_{2n} = [1 + 2\pi p_n(t_0 - \tau)]c_n/[4\pi^2 p_n^2 t_0(1 - 2\pi p_n \tau)], \tag{A10}$$

and

$$C_{3n} = c_n/(1/\tau - 2\pi p_n). \tag{A11}$$

We used the relationship $\sum_{n=1}^{4}(c_n/p_n) = 0$ to derive equation (A8). A simple integration of equation (A8) yields

$$v_{[1]}(t) = \begin{cases} 0 & (t \le 0) \\ \psi_0 g \sum_{n=1}^{4} C_{1n}\{[\exp(2\pi p_n t) - 1]/(2\pi p_n) - t\} & (0 < t \le t_0) \\ \psi_0 g \sum_{n=1}^{4} \left\{ C_{1n} \exp[2\pi p_n t]/(2\pi p_n) \right. & \\ -C_{2n} \exp[2\pi p_n (t - t_0)]/(2\pi p_n) & \\ \left. + C_{3n}\tau \exp[(t - t_0)/\tau] + c_n \tau/(2\pi p_n) \right\} & (t_0 < t \le t_{\max}) \end{cases} \tag{A12}$$

and

$$v_{[2]}(t)/v_{[1]}(t) = \begin{cases} t/2 + \left[\sum_{n=1}^{4} f_{1n}(t)\right] / \left[\sum_{n=1}^{4} f_{2n}(t)\right] & (0 < t \le t_0) \\ \tau + \left[\sum_{n=1}^{4} f_{3n}(t)\right] / \left[\sum_{n=1}^{4} f_{4n}(t)\right] & (t_0 < t \le t_{\max}) \end{cases}, \tag{A13}$$

where

$$f_{1n}(t) = C_{1n}\{1 + \exp(2\pi p_n t) - [1 - \exp(2\pi p_n t)]/(\pi p_n t)\}, \tag{A14}$$

$$f_{2n}(t) = C_{1n}\{1 + [1 - \exp(2\pi p_n t)]/(2\pi p_n t)\}, \tag{A15}$$

$$f_{3n}(t) = (1 - 2\pi p_n \tau) f_{5n}(t)/(4\pi^2 p_n^2) + c_n \tau (t - t_0)/(2\pi p_n) - C_{1n} t_0 (t_0 - 2\tau)/2, \tag{A16}$$

$$f_{4n}(t) = f_{5n}(t)/(2\pi p_n) + C_{3n}\tau \exp[(t - t_0)/\tau] + c_n \tau/(2\pi p_n), \tag{A17}$$

and

$$f_{5n}(t) = C_{1n} \exp[2\pi p_n t] - C_{2n} \exp[2\pi p_n (t - t_0)]. \tag{A18}$$

Acknowledgments

We are grateful to Toshiko Terakawa for useful discussion and comments. We thank Shinichiro Horikawa, Kenjiro Matsuhiro, and Takashi Okuda for helping to obtain the data. We used tilt and seismic records at stations operated by the Japan Meteorological Agency and Nagano Prefecture. We used a digital elevation model and eruptive vent locations estimated by Geospatial Information Authority of Japan. For easy calculations of the IAPWS-95 equation of state of water, we used the NIST Chemistry WebBook developed by the National Institute of Standards and Technology. Comments by two anonymous reviewers helped to improve the manuscript. We hereby clarify that we have no conflicts of interest. Numerical data of the seismic and tilt waveforms and analysis results are available upon request to the corresponding author. This study was supported by the Earthquake Research Institute cooperative research program.

References

Anderson, K., and P. Segall (2011), Physics-based models of ground deformation and extrusion rate at effusively erupting volcanoes, *J. Geophys. Res.*, *116*, B07204, doi:10.1029/2010JB007939.

Aoyama, H., and H. Oshima (2008), Tilt change recorded by broadband seismometer prior to small phreatic explosion of Meakan-dake volcano, Hokkaido, Japan, *Geophys. Res. Lett.*, *35*, L06307, doi:10.1029/2007GL032988.

Bernabe, Y., U. Mok, and B. Evans (2003), Permeability-porosity relationships in rocks subjected to various evolution processes, *Pure Appl. Geophys.*, *160*, 937–960, doi:10.1007/978-3-0348-8083-1_9.

Braun, M. (1993), *Differential Equations and Their Applications*, 4th ed., Springer, New York.

Chouet, B., and P. Dawson (2015), Seismic source dynamics of gas-piston activity at Kilauea Volcano, Hawaii, *J. Geophys. Res. Solid Earth*, *120*(4), 2525–2560, doi:10.1002/2014JB011789.

Chouet, B., and H. R. Shaw (1991), Fractal properties of tremor and gas piston events observed at Kilauea Volcano, Hawaii, *J. Geophys. Res.*, *96*(B6), 10,177–10,189, doi:10.1029/91JB00772.

Christenson, B. W., A. G. Reyes, R. Young, A. Moebis, S. Sherburn, J. Cole-Baker, and K. Britten (2010), Cyclic processes and factors leading to phreatic eruption events: Insights from the 25 September 2007 eruption through Ruapehu Crater Lake, New Zealand, *J. Volcanol. Geotherm. Res.*, *191*(1–2), 15–32, doi:10.1016/j.jvolgeores.2010.01.008.

Fischer, T. P. (2008), Fluxes of volatiles (H_2O, CO_2, N_2, Cl, F) from arc volcanoes, *Geochem. J.*, *42*(1), 21–38.

Gallagher, J. S., R. Crovetto, and J. M. H. Levelt Sengers (1993), The thermodynamic behavior of the CO_2–H_2O system from 400 to 1000 K, up to 100 MPa and 30% mole fraction of CO_2, *J. Phys. Chem. Ref. Data*, *22*(2), 431–513, doi:10.1063/1.555938.

Genco, R., and M. Ripepe (2010), Inflation-deflation cycles revealed by tilt and seismic records at Stromboli volcano, *Geophys. Res. Lett.*, *37*(12), L12302, doi:10.1029/2010GL042925.

Germanovich, L. N., and R. P. Lowell (1995), The mechanism of phreatic eruptions, *J. Geophys. Res.*, *100*(B5), 8417–8434, doi:10.1029/94JB03096.

Greiner, W., L. Neise, and H. Stocker (1995), *Thermodynamics and Statistical Mechanics*, Springer, New York.

Iguchi, M., H. Yakiwara, T. Tameguri, M. Hendrasto, and J. Hirabayashi (2008), Mechanism of explosive eruption revealed by geophysical observations at the Sakurajima, Suwanosejima and Semeru volcanoes, *J. Volcanol. Geotherm. Res.*, *178*(1), 1–9, doi:10.1016/j.jvolgeores.2007.10.010.

Ikehata, K., and T. Maruoka (2016), Sulfur isotopic characteristics of volcanic products from the September 2014 Mount Ontake eruption, Japan, *Earth Planets Space*, *68*, 116, doi:10.1186/s40623-016-0496-z.

Julian, B. R. (1994), Volcanic tremor: Nonlinear excitation by fluid flow, *J. Geophys. Res.*, *99*(B6), 11859–11877, doi:10.1029/93JB03129.

Kato, A., T. Terakawa, Y. Yamanaka, Y. Maeda, S. Horikawa, K. Matsuhiro, and T. Okuda (2015), Preparatory and precursory processes leading up to the 2014 phreatic eruption of Mount Ontake, Japan, *Earth Planets Space*, *67*, 111, doi:10.1186/s40623-015-0288-x.

Konstantinou, K. I. (2002), Deterministic non-linear source processes of volcanic tremor signals accompanying the 1996 Vatnajokull eruption, central Iceland, *Geophys. J. Int.*, *148*(3), 663–675, doi:10.1046/j.1365-246X.2002.01608.x.

Kozono, T., and T. Koyaguchi (2012), Effects of gas escape and crystallization on the complexity of conduit flow dynamics during lava dome eruptions, *J. Geophys. Res.*, *117*(B8), B08204, doi:10.1029/2012JB009343.

Maeda, Y., M. Takeo, and T. Ohminato (2011), A waveform inversion including tilt: Method and simple tests, *Geophys. J. Int.*, *184*(2), 907–918, doi:10.1111/j.1365-246X.2010.04892.x.

Maeda, Y., A. Kato, T. Terakawa, Y. Yamanaka, S. Horikawa, K. Matsuhiro, and T. Okuda (2015), Source mechanism of a VLP event immediately before the 2014 eruption of Mt. Ontake, Japan, *Earth Planets Space*, *67*, 187, doi:10.1186/s40623-015-0358-0.

Maeno, F., S. Nakada, T. Oikawa, M. Yoshimoto, J. Komori, Y. Ishizuka, Y. Takeshita, T. Shimano, T. Kaneko, and M. Nagai (2016), Reconstruction of a phreatic eruption on 27 September 2014 at Ontake volcano, central Japan, based on proximal pyroclastic density current and fallout deposits, *Earth Planets Space*, *68*, 82, doi:10.1186/s40623-016-0449-6.

Melnik, O., and R. S. J. Sparks (2005), Controls on conduit magma flow dynamics during lava dome building eruptions, *J. Geophys. Res.*, *110*, B02209, doi:10.1029/2004JB003183.

Mogi, K. (1958), Relations between the eruptions of various volcanoes and the deformations of the ground surfaces around them, *Bull. Earthquake Res. Inst.*, *36*(2), 99–134.

Nakamichi, H., H. Kumagai, M. Nakano, M. Okubo, F. Kimata, Y. Ito, and K. Obara (2009), Source mechanism of a very-long-period event at Mt. Ontake, central Japan: Response of a hydrothermal system to magma intrusion beneath the summit, *J. Volcanol. Geotherm. Res.*, *187*(3–4), 167–177, doi:10.1016/j.jvolgeores.2009.09.006.

Nishimura, T. (2009), Ground deformation caused by magma ascent in an open conduit, *J. Volcanol. Geotherm. Res.*, *187*(3–4), 178–192, doi:10.1016/j.jvolgeores.2009.09.001.

Nishimura, T., M. Iguchi, R. Kawaguchi, M. H. Surono, and U. Rosadi (2012), Inflations prior to Vulcanian eruptions and gas bursts detected by tilt observations at Semeru Volcano, Indonesia, *Bull. Volcanol.*, *74*(4), 903–911, doi:10.1007/s00445-012-0579-z.

Ogiso, M., H. Matsubayashi, and T. Yamamoto (2015), Descent of tremor source locations before the 2014 phreatic eruption of Ontake volcano, Japan, *Earth Planets Space*, *67*, 206, doi:10.1186/s40623-015-0376-y.

Okada, Y. (1992), Internal deformation due to shear and tensile faults in a half-space, *Bull. Seismol. Soc. Am.*, *82*(2), 1018–1040.

Rodgers, P. W. (1968), The response of the horizontal pendulum seismometer to Reileigh and Love waves, tilt, and free oscillations of the Earth, *Bull. Seismol. Soc. Am.*, *58*(5), 1385–1406.

Takagi, A., and S. Onizawa (2016), Shallow pressure sources associated with the 2007 and 2014 phreatic eruptions of Mt. Ontake, Japan, *Earth Planets Space*, *68*, 135, doi:10.1186/s40623-016-0515-0.

Tameguri, T., M. Iguchi, H. Nakamichi, and K. Yamamoto (2016), Disaster research of Kuchinoerabujima eruptions in 2014–2015 [in Japanese with English abstract], *Ann. Disast. Prev. Res. Inst.*, *59*, 85–90.

Terada, A. (2014), *Heat-Discharge Activities From the Jigokudani Crater at Ontake Volcano After the Phreatic Eruption in September 2014 [in Japanese]*, paper presented at 2014 Fall Meeting, The Volcanological Society of Japan, Fukuoka, Japan.

Terakawa, T., A. Kato, Y. Yamanaka, Y. Maeda, S. Horikawa, K. Matsuhiro, and T. Okuda (2016), Monitoring eruption activity using temporal stress changes at Mount Ontake Volcano, *Nat. Commun.*, *7*(10), 797, doi:10.1038/ncomms10797.

Turcotte, D. L., and G. Schubert (2002), *Geodynamics*, 2nd ed., Cambridge Univ. Press, New York.

Vandemeulebrouck, J., et al. (2014), Eruptions at Lone Star geyser, Yellowstone National Park, USA: 2. Constraints on subsurface dynamics, *J. Geophys. Res. Solid Earth*, *119*(12), 8688–8707, doi:10.1002/2014JB011526.

Wagner, W., and A. Pruss (2002), The IAPWS formulation 1995 for the thermodynamic properties of ordinary water substance for general and scientific use, *J. Phys. Chem. Ref. Data*, *31*(2), 387–535, doi:10.1063/1.1461829.

Yamamoto, T., Y. Nakamura, and H. Glicken (1999), Pyroclastic density current from the 1888 phreatic eruption of Bandai volcano, NE Japan, *J. Volcanol. Geotherm. Res.*, *90*(3–4), 191–207, doi:10.1016/S0377-0273(99)00025-6.